

## Article

# Corrosion Resistance of Cr–Co Alloys Subjected to Porcelain Firing Heat Treatment—In Vitro Study

Dorota Rylska <sup>1</sup>, Bartłomiej Januszewicz <sup>1,\*</sup>, Grzegorz Sokołowski <sup>2</sup> and Jerzy Sokołowski <sup>3</sup>

<sup>1</sup> Institute of Materials Science and Engineering, Lodz University of Technology, 90-924 Lodz, Poland; dorota.rylska@p.lodz.pl

<sup>2</sup> Department of Prosthetics, Medical University of Lodz, 92-213 Lodz, Poland; grzegorz.sokolowski@umed.lodz.pl

<sup>3</sup> Department of General Dentistry, Medical University of Lodz, 92-213 Lodz, Poland; jerzy.sokolowski@umed.lodz.pl

\* Correspondence: bartlomiej.januszewicz@p.lodz.pl; Tel.: +48-42-6313050 or +48-663-457-566

**Abstract:** The procedure of ceramics fusion to cobalt–chromium (Co–Cr) base dental crowns affects their corrosion behavior and biological tolerance. This study’s purpose was to comparatively evaluate the effect of heat treatment (HT) applicable for dental ceramics firing on the corrosion properties among Co–Cr base alloys fabricated via different methods: casting (CST), milling soft metal and post sintering (MSM), and selective laser melting (SLM). All specimens were subjected to a heat treatment corresponding to a full firing schedule. The microstructure and elemental composition of oxidized surfaces were investigated by scanning electron microscopy and energy dispersive spectroscopy. Corrosion properties were examined by electrochemical potentiodynamic polarization tests. The values of  $j_{corr}$ ,  $E_{corr}$ ,  $R_p$ , and breakdown potential  $E_{br}$  were estimated. The oxide layers formed during the HT process corresponded to the composition of the original alloys’ structure. Among the thermal treated alloys, SLM showed the highest corrosion resistance, followed by the MSM and CST. This may be attributed to uniform distribution of alloying elements in homogenous structure and to the reduced porosity, which enhances corrosion resistance and decreases the risk of crevice corrosion. The overall corrosion behavior was strongly influenced by the segregation of alloying elements in the microstructure, thus, is directly determined by the manufacturing method.

**Keywords:** Co–Cr dental alloys; corrosion; porcelain firing; SLM; MSM; CST



**Citation:** Rylska, D.; Januszewicz, B.; Sokołowski, G.; Sokołowski, J. Corrosion Resistance of Cr–Co Alloys Subjected to Porcelain Firing Heat Treatment—In Vitro Study. *Processes* **2021**, *9*, 636. <https://doi.org/10.3390/pr9040636>

Academic Editors: Lukáš Richtera and Leszek Dobrzański

Received: 17 February 2021

Accepted: 26 March 2021

Published: 5 April 2021

**Publisher’s Note:** MDPI stays neutral with regard to jurisdictional claims in published maps and institutional affiliations.



**Copyright:** © 2021 by the authors. Licensee MDPI, Basel, Switzerland. This article is an open access article distributed under the terms and conditions of the Creative Commons Attribution (CC BY) license (<https://creativecommons.org/licenses/by/4.0/>).

## 1. Introduction

Currently, despite the growing popularity of all-ceramic restorations, a significant number of prosthetic works are made using the method of ceramics fusion on metal. Metal–ceramic restorations are used most frequently for fixed partial dentures and single crowns because of the good mechanical properties of alloys as well as the aesthetic characteristics of porcelain. Due to the high cost of noble metal alloys, base metal alloys, such as cobalt–chromium (Co–Cr), are more extensively used for the metal–ceramic restorations’ construction. The low density, high hardness, and tensile strength [1] make base metal alloys superior to noble metals. The most popular technique is lost-wax casting, although there are also several dental technologies for manufacturing a final product from cobalt–chrome base alloys as alternatives to traditional casting techniques. These alternative methods include the milling of solid metal, milling in soft material, and sintering in a protective atmosphere (MSM) and selective laser melting (SLM) [2–4]. The milling alloys (1) are not likely to indicate procedural errors, such as impurities and shape deformations as a result of thermal tension and (2) show lower corrosion susceptibility than alloys manufactured by casting (CST) [5].

The effective and durable methods of improvement in corrosion resistance are still in great demand, because commonly applied dental alloys, like Co–Cr base alloys, are prone

to corrosion in contact with physiological fluids. Impairment or destruction of the thin protective oxide layer on their surface, mostly composed of Cr oxide, is reported as the main reason for corrosion resistance reduction [6,7]

The metallic materials may be subjected to electrochemical pitting and crevice, fretting and fatigue corrosion, and stress corrosion cracking. The presence of chloride ions in an environment with a relatively high temperature (37 °C) is a significant cause of these alloys' corrosion. Moreover, frequently changing conditions in an oral cavity (e.g., the presence of food, pH changes, and bacteria [8]) are very harmful.

The corrosion does not only affect the metallic elements of prostheses in direct contact with saliva. It also occurs in the space of the metal inlay connection with the porcelain facing [9]. Most importantly, corrosion concerns the internal surface of metal–ceramic crowns since none of the prosthetic cements used for crown and bridge imbedding assures the connection is suitably tight. In effect, the electrolytic environment of the oral cavity penetrates and stays in contact with a metal surface (the crown's interior), causing crevice corrosion processes.

The corrosion of base alloys commences with the localized destruction of the passive layer, enabling the corrosive environment to penetrate the alloy and to cause damage to its structure. The mechanism and extent of the damage depend on the chemical composition of the alloy used. The second factor is the alloy's internal structure, conditioned by the manufacturing method.

Apart from various functional and technical advantages, the CST alloys have several drawbacks typical for casting, such as a microporosity, a tendency towards a coarse crystalline structure, dendritic microsegregation, and the coarse-grained precipitation of intermetallic phases and carbides. The foregoing detriments undoubtedly result in more critical pitting and galvanic corrosion [10–12].

The procedures of ceramics fusion on metal, which include

- surface oxidation,
- opaque ceramics fusion,
- dentin and enamel ceramics fusion, and
- glaze fusion.

Involve oxidation of the metallic surface and scale formation may affect the corrosion properties and thus the biological properties of metallic material [9,13,14].

New processing methods developed for cobalt and chrome-based alloys, not only fulfil the requirements of rapid manufacturing (RM) and rapid prototyping (RP), reduce the design lifecycle, and lower the cost of medical devices [15,16], but also help to increase the corrosion resistance of these materials, hence ensuring greater biocompatibility.

The literature includes many studies describing SLM technology, as well as comparative studies evaluating the mechanical properties, structure, and corrosion susceptibility of SLM alloys in comparison to the properties of cast elements made with the same metallic materials. The results of the studies demonstrate that the SLM elements have better properties than the ones obtained by the traditional casting methods, because of the equality of the SLM alloys' structures [17,18].

The latest technique (MSM) involves producing restorations with powder metallurgy methods [19,20]. This method seems to allow for a more homogeneous product, with a stable structure and with improved ductility compared with the traditional Co–Cr cast alloys [21].

The electrochemical characteristic of the cast and SLM-produced parts of dental Co–Cr base alloys have been extensively tested, but there are limited data concerning MSM technology. The literature on the last MSM study was considerably poorer and mainly includes studies on the fracture behavior of metal–ceramic bridges with Co–Cr–Mo frameworks obtained by powder metallurgy methods [20,22].

The studies concerning porcelain-fused-to-metal (PFM) Co–Cr dental alloys have mainly been concentrated on the evaluation of the marginal and/or internal fit of the restorations [23], whereas other studies performed an evaluation of the mechanical prop-

erties and porcelain bond strength [5,24,25], the effect of surface treatments on micro-roughness [25,26], the impact of the surface finishing process on the metal–ceramic bond strength, and the impact of different factors on the pre-oxidation process conducted before the PFM dental crown was fabricated [27–31].

In light of the results of previous research, it is not unfounded to state that the effect of the heat treatment (HT) assisting the porcelain fusion on corrosion occurrence in dental Co–Cr base alloys needs further investigation. Understanding whether and how the microstructure of metallic parts of crowns can affect their corrosion behavior after procedures of ceramics fusion in an oral cavity environment constitutes a key issue from a clinical perspective.

The aim of this study was to comparatively evaluate the effect of the thermal treatment applicable for dental ceramics firing on the surface characteristics, mainly the corrosion resistance of Co–Cr base alloys fabricated via the use of casting and two computer-aided design and manufacturing methods: milling soft metal and post-sintering (MSM) and selective laser melting (SLM). The null hypothesis was that no significant difference would be found among the alloys manufactured by different techniques after the heat treatment applied.

## 2. Materials and Methods

### 2.1. Materials Used and Processing

Five alloys (CST1, CST2, MSM, SLM1, and SLM2), each of three samples, were prepared.

In the CST group, alloys from Ceranium CC (CST1), produced by Mesa di Sala Giacomo & C. s.n.c., Italy, and Girobond NBS Co–Cr (CST2, produced by Amann Girrbach, Austria, were manufactured with the rotational method in a Formax induction-casting machine (Bego GmbH, Bremen, Germany).

The obtainment of elements produced from milled powder blocks made of Co–Cr alloys bonded with a binding agent (Ceramill Sintron/Amann Girrbach, Dresden, Germany) and sintered in a Ceramil Argotherm furnace in an inert gas environment was followed by sinterization (MSM). The Ceramil Sintron samples were dry-milled in a process involving dust extraction using a four-axis milling CNC machine (Amann Girrbach Motion). The sintering process was performed in the Ceramil Argotherm furnace in an argon atmosphere at 1300 °C according to the manufacturer’s instructions (sintering program duration: approximately 5 h).

The two kinds of SLM specimens were prepared from Co–Cr powders. The SLM1 alloy was produced from Modelstar S Powder 65 (Scheftner, Maintz, Germany) by using a dental laser-sintering device Realizer SLM100, (Realizer GmbH, Borhen, Germany).

The second SLM alloy (SLM2) was made from a Co–Cr alloy (similar in composition to the Starbond COS Powder (Scheftner, Maintz, Germany) using the Realizer SLM50 (Realizer GmbH, Borhen, Germany), but with an increased content of Mo and a decreased content of W (see Table 1). The composition (by weight) of all specimens is given in Table 1.

**Table 1.** Chemical composition (by wt %) of examined samples.

Sample	Co	Cr	W	Mo	Si	Others
CST 1	60.0	28.0	9.0	-	1.5	Mn, Fe < 1%.
CST 2	62.4	25.5	5.2	5.1	1.1	Nb, Fe, N < 1%.
MSM	66.0	28.0	-	5.0	-	Mn, Si, Fe < 1%; Organic binder: 1–2%.
SLM 1	62.7	28.8	-	6.0	0.7	C, Fe, Si, Mn < 1%.
SLM 2	58.5	25.3	7.3	6.6	0.9	Mn 0.8%; Fe < 1%.

All samples for further examinations, prepared as drilled discs with a diameter of 14 mm and a height of 7 mm, were wet grinded with abrasive papers up to P2400, and their surface was then treated with a 3- $\mu$ m diamond polisher. Degreased and water-vapor-steam-cleaned specimens were exposed to a thermal treatment simulating the full firing

schedule of a matched dental porcelain in a porcelain furnace Programat EP 3000 (Ivoclar Vivadent, Amherst, NY, USA).

### 2.2. Heat Treatment Simulating Porcelain Firing Processes

All specimens were brought under a full firing schedule (following Noritake—Super Porcelain EX3, Kuraray Noritake Inc. Japan) including two opaque, two dentine, and one final glaze simulating firings in a porcelain furnace—Ivoclar Vivadent Programat EP3000 (Ivoclar Vivadent, Amherst, NY, USA).

Particular processes of the HT corresponded to Noritake EX-3 ceramics are presented in Table 2.

**Table 2.** Processes of the applied heat treatment (HT).

Process	Opaque 1	Opaque 2	Dentine 1	Dentine 2	Final Glaze
B	400 °C	650 °C	600 °C	600 °C	650 °C
S	8 min	5 min	7 min	10 min	5 min
V1	400 °C	650 °C	600 °C	600 °C	-
t <sub>1</sub>	65 °C/min	55 °C/min	45 °C/min	45 °C/min	55 °C/min
T	1000 °C	945 °C	935 °C	935 °C	910 °C
V2	1000 °C	935 °C	920 °C	925 °C	-
H	1 min	-	-	-	-

B = Initial temperature; S = Time for drying and furnace chamber closing; V1 = Temperature of vacuum activation; t<sub>1</sub> = Speed of temperature's increase; T = Firing temperature; V2 = Temperature of vacuum deactivation; H = Warming up time.

### 2.3. Microstructure and Chemical Characterization

For the microstructural characterization, the specimens of each group were examined using a SEM (scanning electron microscope) JEOL JSM-6610LV (JEOL, Akashima Tokyo, Japan) and performing EDS (Energy Dispersive X-Ray Spectroscopy) analysis.

Cross sections of oxidized samples were prepared to determine the thickness of the oxides (shown in Table 3).

**Table 3.** The average thickness of oxide layers covered the examined alloys.

Sample	CST1	CST2	MSM	SLM1	SLM2
Average oxide thickness [μm]	1.59	1.59	1.25	1.61	1.26

In consideration of the above data and the oxides' brittleness, surface SEM-EDS examinations were conducted. The influence of the base material could be neglected because of the following:

- The thickness of the oxide layers varied in the range of 1.16–1.78 μm.
- The average atomic mass of the elements creating the oxides is high, which directly affects the depth of penetration of the primary electron beam.

The examined surfaces were imaged under an accelerating voltage of 20 kV. The microanalyses of the chemical composition were performed with an EDS X-MAX 80 microanalyzer (Oxford Instruments, High Wycombe, UK) under an accelerating voltage of 20 kV. According to the EDS method, we performed a qualitative and quantitative analysis of the chemical composition (both the elemental constituents and oxides) of selected areas and points, and along the selected lines. The surfaces of all samples were also subjected to SEM-SE observations after electrochemical examinations. Additionally, the SEM/EDS examinations were performed for the samples subjected to the corrosion investigations.

The microstructure of the alloys before the HT was investigated by SEM-SE, and the surface distributions of the elements for all specimens before the HT were determined by the energy-dispersive X-ray spectroscopy method under the same accelerating voltage.

#### 2.4. Corrosion Properties Examinations

The corrosion susceptibility was investigated by employing potentiodynamic polarization. The electrochemical tests were performed for all samples subjected to the HT simulating porcelain firing at room temperature in a 0.9% NaCl solution (ASTM F746-04(2014) Standard Test Method for Pitting or Crevice Corrosion of Metallic Surgical Implant Materials).

The corrosion resistance of the samples was assessed with an Atlas 0531 Electrochemical Unit & Impedance Analyzer kit. It consisted of a five-electrode accessory for measuring the chrono-volt amperometric curves of electrochemical systems consistent with AtlasCorr software (Atlas-Sollich, Rebiechowo-Gdańsk, Poland). An electrochemical cell (CEC/TH Thermostated Multipurpose Cell—Radiometer Analytical, Lyon, France) and a three-electrode measuring system were used for the corrosion tests (CT).

After being ultrasonically rinsed in double distilled water and ethanol for 10 min, respectively, three samples of each kind were placed in a special holder as a working electrode; the exposed surface area was equal to 0.95 cm<sup>2</sup>. A platinum electrode served as a counter electrode, and a saturated calomel electrode (SCE) served as a reference electrode. The corrosion cell was a 250-mL vessel with a thermo-stating jacket. The working and platinum electrodes were mounted on the sides, facing each other; the SCE electrode was connected with the working electrode through a bridge with a Luggin capillary. The capillary tip was positioned within 2 mm of the working electrode surface to reduce the ohm drop of the solution. The specimens were exposed to the solution for 1 h to establish an open circuit potential (OCP), and potentiodynamic polarization scans were applied after establishing the OCP. The potentiodynamic polarization curves were recorded by scanning from an initial potential of −1.0 V vs. the OCP (which was measured with reference to the SCE) to a final potential of 2.0 V vs. the OCP at a scanning rate of 5 mV/s. We employed the Tafel extrapolation method, in the domain of the ±200 mV SCE vs. the OCP, to determine the corrosion current  $i_{\text{corr}}$  and the corrosion potential  $E_{\text{corr}}$ . The values of  $j_{\text{corr}}$  and  $E_{\text{corr}}$  were obtained by means of extrapolation of the Tafel straights. The areas of potentiodynamic curves assumed as Tafel straights were chosen manually to avoid mistakes in interpretation generated by the commercial software. Analysis was performed by extrapolating the linear portions of a logarithmic current vs. a potential plot back to their intersection.

The potential ( $E_{\text{br}}$ ), at which the corrosion current increases abruptly, was also estimated from the polarization curves (at potentials below the oxygen-evolution potential when the neutral saline solution was ~0.6 V).

#### 2.5. Statistical Analysis

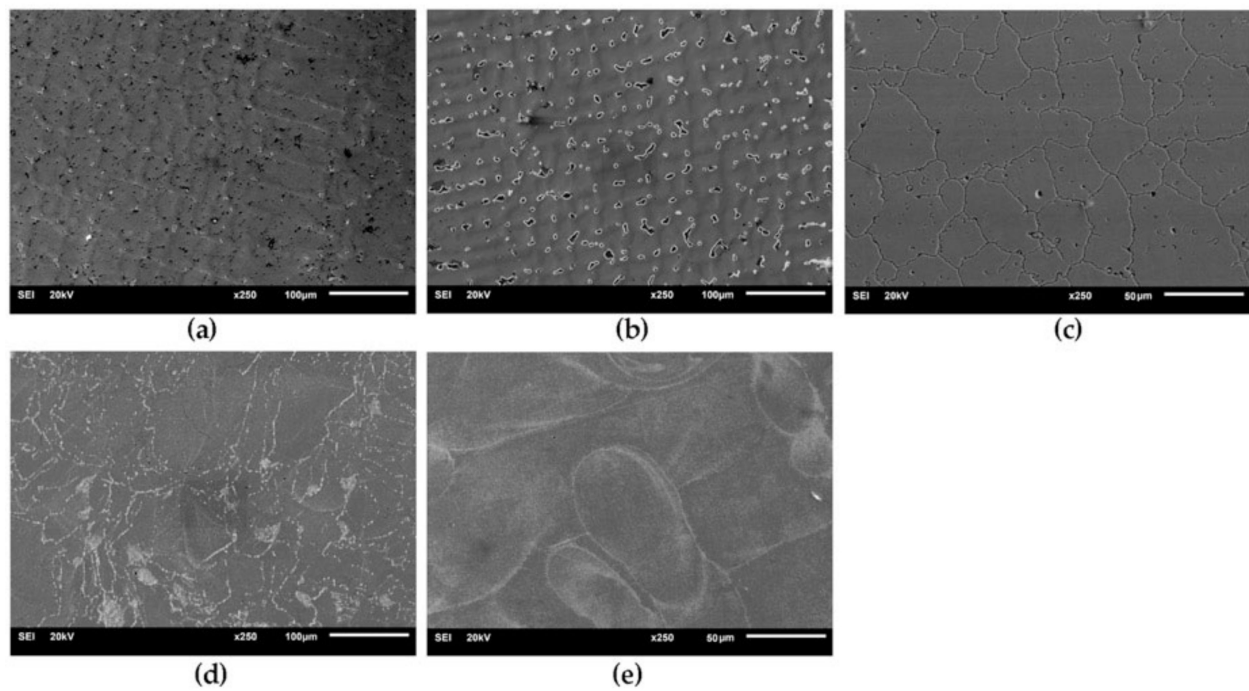
One-way analysis of variance (ANOVA) was used for the data of  $j_{\text{corr}}$ ,  $E_{\text{corr}}$ ,  $R_p$ , and  $E_d$ , followed by a Tukey post-hoc test ( $\alpha = 0.05$ ).

### 3. Results

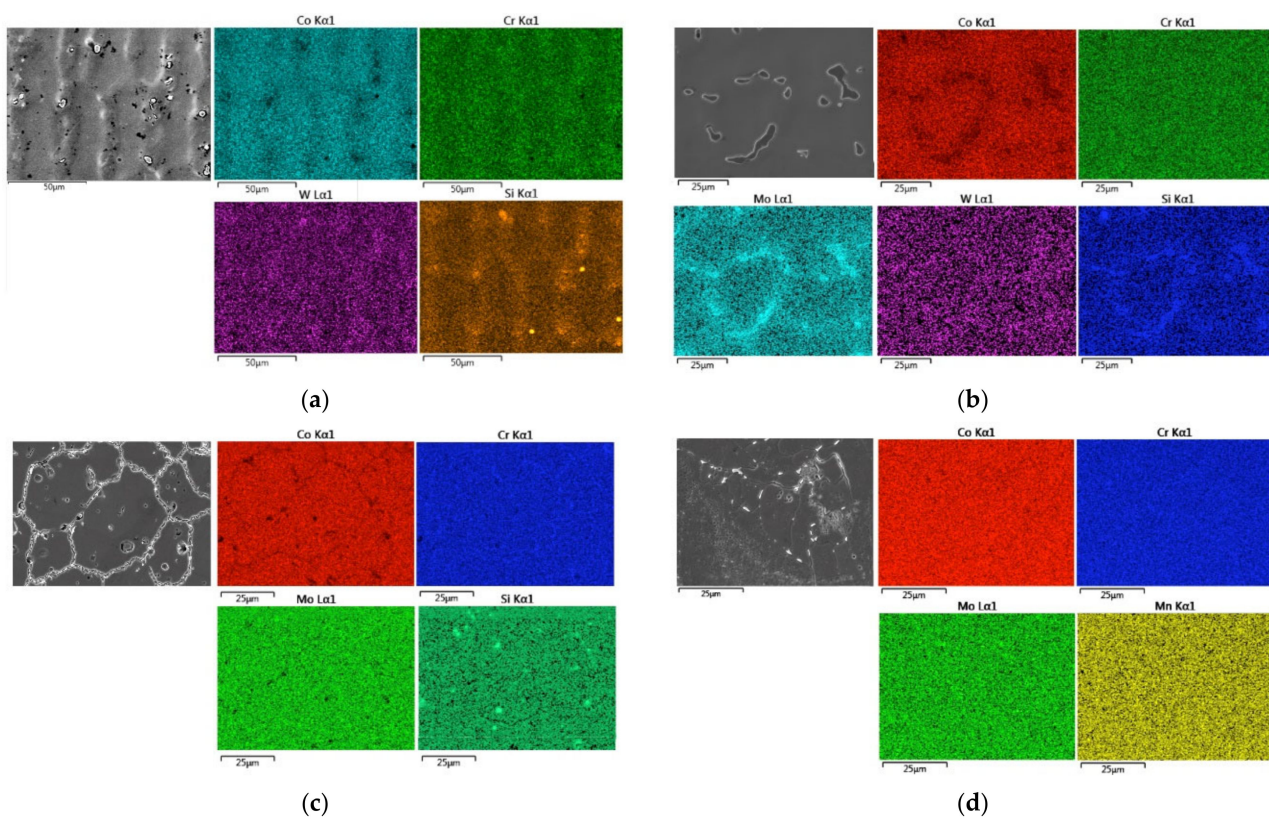
#### 3.1. Microstructure and Chemical Characterization

Figure 1a–e presents the microstructure of all examined alloys before the thermal treatment. The SEM-SE with corresponding EDS mapping images for each alloy (before the HT) is shown in Figure 2a–f.

The results of the morphology examinations and tests, determining the chemical composition of the surface layers of the heat-treated elements, are presented below in Figures 3–7. The (a) panel of each figure shows the morphology of the sample's surface obtained by using a scanning microscope in a secondary electrons (SE) mode supplemented by the quantitative results of the average chemical composition (both elements and oxides) from the selected area. The EDS maps presenting the surface distribution of elements are shown in the (b) panel of each figure. The next panel, (c), presents the results of quantitative EDS examinations for the representative points (marked in the SEM-SE image). The (d) panel presents the EDS results of the relative concentration of elements along the selected line.



**Figure 1.** SEM-SE (Secondary Electrons) images of the Co–Cr alloys before the heat treatment (HT). (a) CST1; (b) CST2; (c) MSM; (d) SLM1; (e) SLM2.



**Figure 2.** Cont.

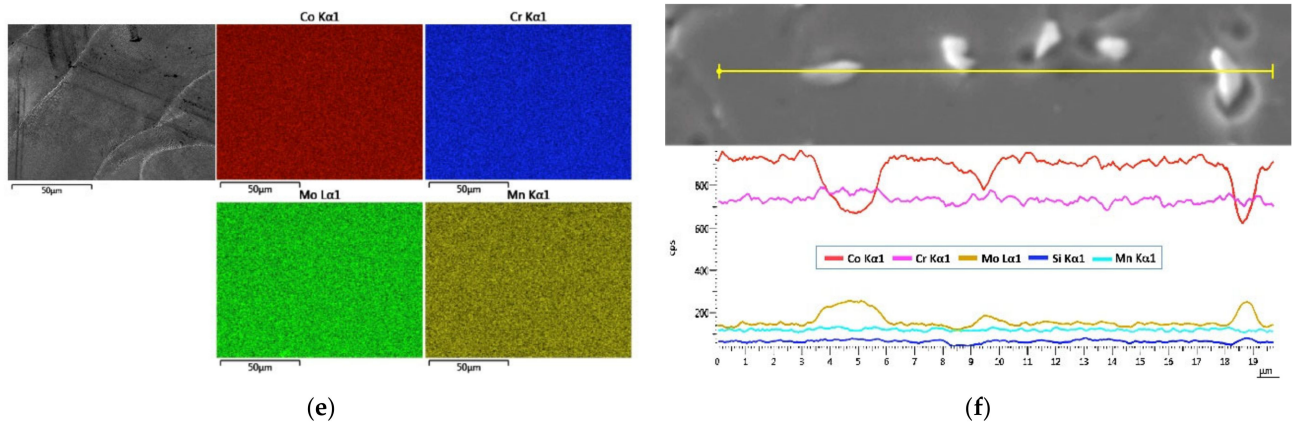
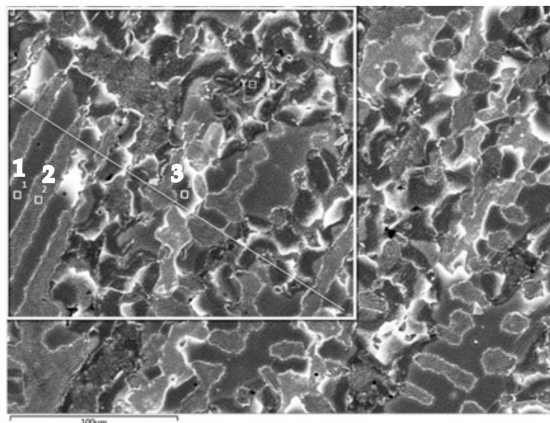


**Figure 2.** SEM-SE and corresponding EDS mapping images for each alloy before the HT (a–e): (a) CST1 with Co, Cr, W, and Si distributions; (b) CST2 with Co, Cr, Mo, W, and Si distributions; (c) MSM with Co, Cr, Mo, and Si distributions; (d) SLM1 with Co, Cr, Mo, and Mn distributions; (e) SLM2 with Co, Cr, Mo, and Mn distributions; (f) SLM1 SEM-SE micrograph with corresponding EDS line scan results from the grain boundary area with bright precipitations.



Element	wt %	Oxide	Oxide wt %
O	25.74		
Si	1.21	SiO <sub>2</sub>	2.59
Cr	24.1	Cr <sub>2</sub> O <sub>3</sub>	35.23
Co	43.86	CoO	55.76
W	5.09	WO <sub>3</sub>	6.42
Total:	100		100

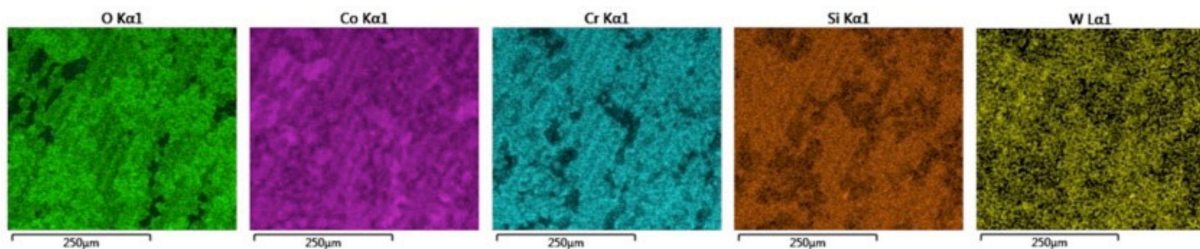


**Figure 3.** Cont.

Element [wt %]	1	2	3	Oxide [wt %]	1	2	3
O	25.85	26.29	26.33				
Si	1.02	2.58	0.85	SiO <sub>2</sub>	2.19	5.52	1.82
Cr	25.73	21.58	29.67	Cr <sub>2</sub> O <sub>3</sub>	37.6	31.53	43.37
Co	41.83	43.37	38.04	CoO	53.19	55.15	48.37
W	5.56	6.18	5.11	WO <sub>3</sub>	7.02	7.8	6.44
Total:	100	100	100		100	100	100

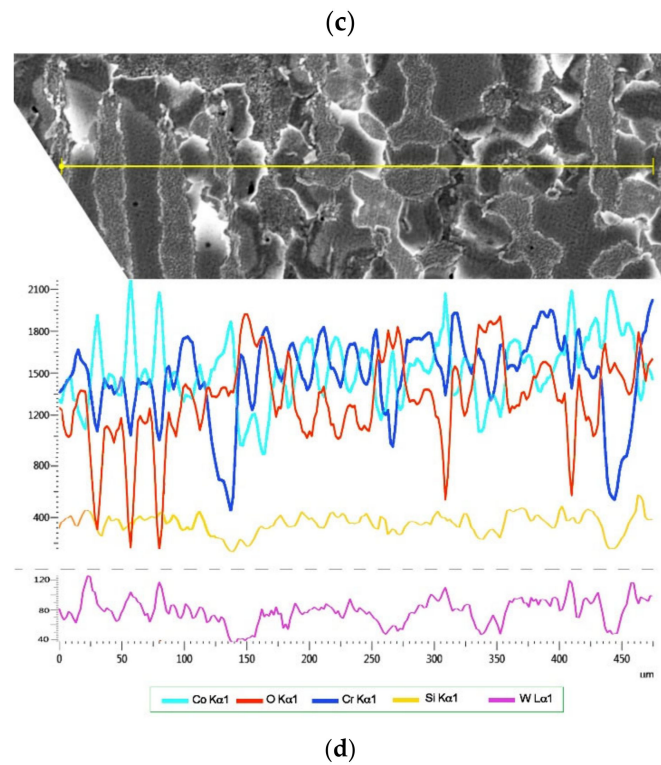
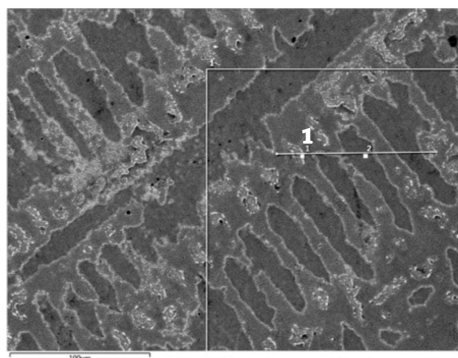


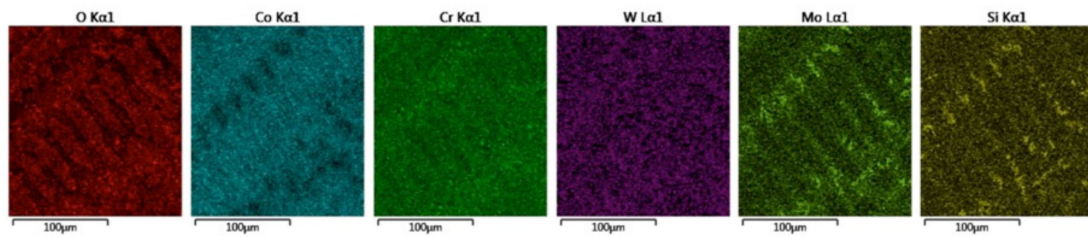
**Figure 3.** SEM EDS results for the CST1 sample: (a) SEM-SE morphology with average EDS results from the marked area; (b) maps presenting the surface distribution of O, Co, Cr, W, and Si; (c) EDS results for marked points; (d) SEM-SE micrograph with corresponding EDS line scan results.



Element	wt %	Oxide	Oxide wt %
O	26.47		
Si	1.45	SiO <sub>2</sub>	3.1
Cr	23.15	Cr <sub>2</sub> O <sub>3</sub>	33.83
Co	41.1	CoO	52.26
Mo	3.88	MoO <sub>3</sub>	5.82
W	3.96	WO <sub>3</sub>	4.99
Total:	100		100

(a)

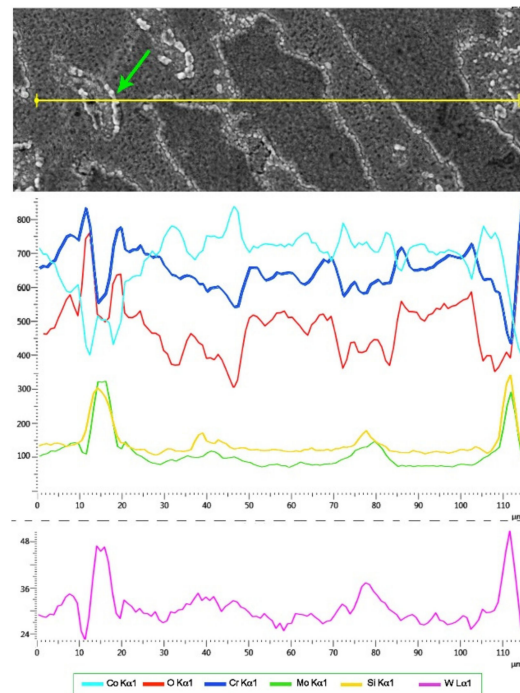
**Figure 4.** Cont.



(b)

Element [wt %]	Point 1	Point 2	Oxide [wt %]	Point 1	Point 2
O	29.92	25.83			
Si	2.23	1.28	SiO <sub>2</sub>	4.78	2.73
Cr	43.79	20.85	Cr <sub>2</sub> O <sub>3</sub>	64	30.47
Co	19.52	45.79	CoO	24.82	58.23
Mo	2.84	2.87	MoO <sub>3</sub>	4.27	4.3
W	1.69	3.39	WO <sub>3</sub>	2.13	4.27
Total:	100	100		100	100

(c)



(d)

**Figure 4.** SEM EDS results for the CST2 sample: (a) SEM-SE micrograph showing the morphology with average EDS results from the marked area; (b) maps presenting the surface distribution of O, Co, Cr, W, Mo, and Si; (c) EDS results for marked points; (d) SEM-SE micrograph with corresponding EDS line scan results.

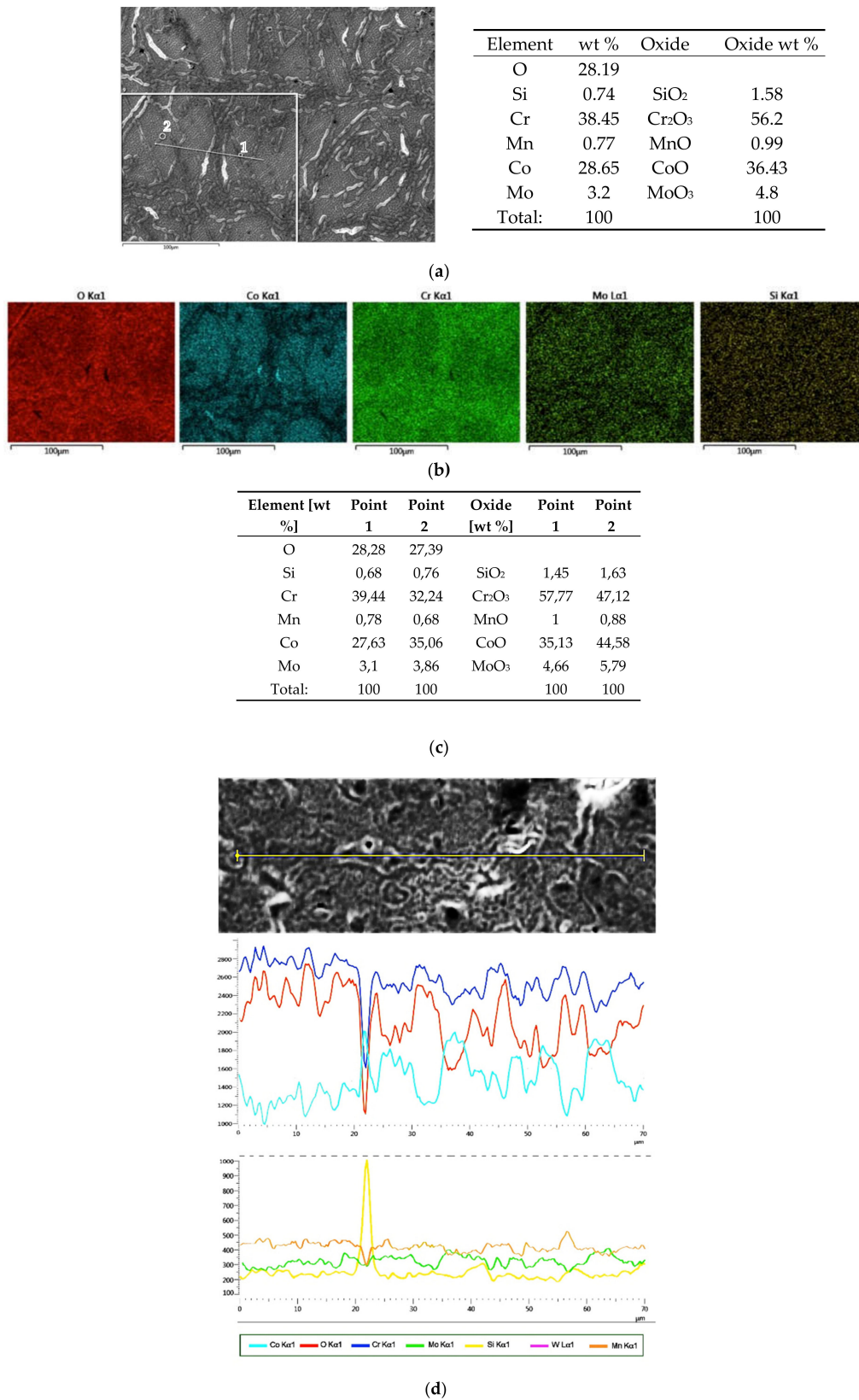


**Figure 5.** SEM EDS results for the MSM sample: (a) SEM-SE micrograph showing the morphology with average EDS results from the marked area; (b) maps presenting the surface distribution of O, Co, Cr, Mo, and Si; (c) EDS results for marked points; (d) SEM-SE micrograph with corresponding EDS line scan results.

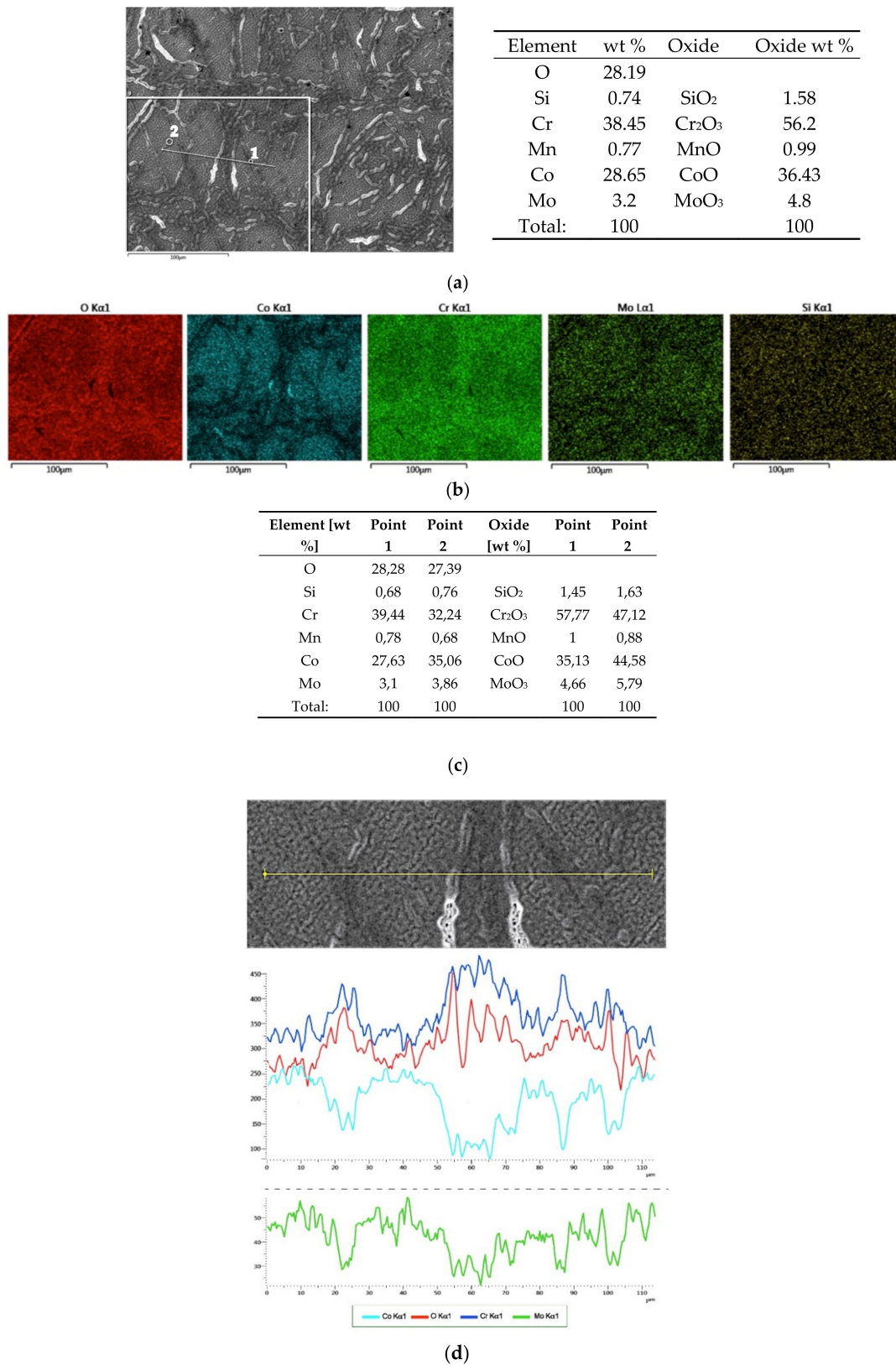
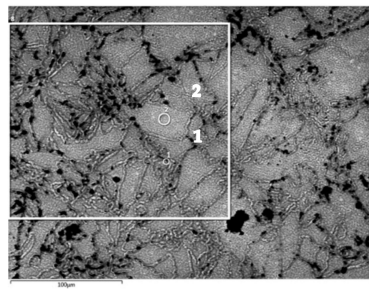
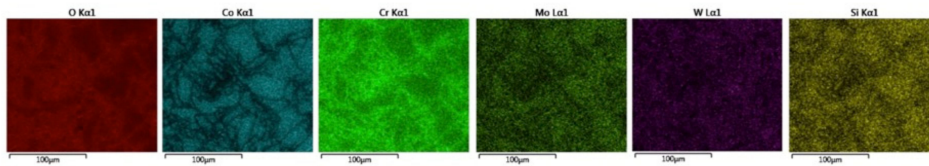


**Figure 6.** SEM EDS results for the SLM1 sample: (a) SEM-SE micrograph showing the morphology with average EDS results from the marked area; (b) maps presenting the surface distribution of O, Co, Cr, Mo, and Si; (c) EDS results for marked points; (d) SEM-SE micrograph with corresponding EDS line scan results.



Element	wt %	Oxide	Oxide wt %
O	27.78		
Si	1.31	SiO <sub>2</sub>	2.8
Cr	33.81	Cr <sub>2</sub> O <sub>3</sub>	49.47
Mn	1.18	MnO	1.52
Co	28.94	CoO	36.74
Mo	3.04	MoO <sub>3</sub>	4.55
W	3.93	WO <sub>3</sub>	4.9
Total:	100		100

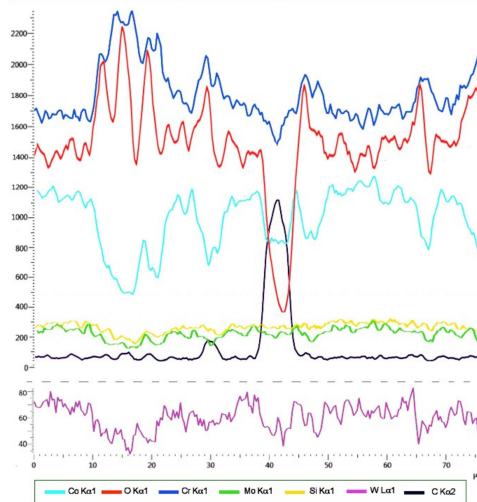
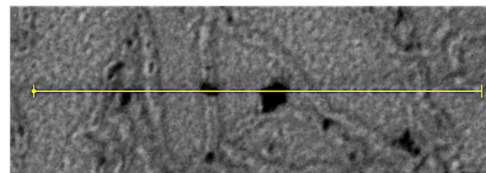
(a)



(b)

Element [wt %]	Point 1	Point 2	Oxide [wt %]	Point 1	Point 2
O	27.67	26.65			
Si	1.2	1.32	SiO <sub>2</sub>	2.57	2.83
Cr	33.23	24.39	Cr <sub>2</sub> O <sub>3</sub>	48.57	35.65
Mn	1.25	0.83	MnO	1.61	1.07
Co	30.03	37.98	CoO	38.19	48.29
Mo	2.98	4.3	MoO <sub>3</sub>	4.47	6.46
W	3.64	4.52	WO <sub>3</sub>	4.59	5.7
Total:	100	100		100	100

(c)



(d)

**Figure 7.** SEM EDS results for the SLM2 sample: (a) SEM-SE micrograph showing the morphology with average EDS results from the marked area; (b) maps presenting the surface distribution of O, Co, Cr, W, Mo, and Si; (c) EDS results for marked points; (d) SEM-SE micrograph with corresponding EDS line scan results.

Table 4. contains data summarizing the contribution of particular oxides covering the surface of thermally treated alloys (based on the quantitative EDS results concerning the average oxides contribution (panels (a) of Figures 3–7)).

**Table 4.** Oxide content on the alloys' surface after the HT process.

Oxide [wt %]	CST1	CST2	MSM	SLM1	SLM2
CoO	55.76	52.26	41.1	36.43	36.74
Cr <sub>2</sub> O <sub>3</sub>	35.23	33.83	49.6	56.2	49.47
MoO <sub>3</sub>	-	5.82	5.24	4.8	4.55
SiO <sub>2</sub>	2.59	3.1	2.28	1.58	2.8
WO <sub>3</sub>	6.42	4.99	-	-	4.9
MnO	-	-	1.78	0.99	1.52

According to Table 4, one can state that the average amount of Cr<sub>2</sub>O<sub>3</sub> covering surfaces after the HT was the highest using both SLM alloys, decreased using MSM samples, and reached the lowest amount using CST alloys.

The (a) panels of Figures 3–7 show the SEM-SE images of the oxidized surfaces representing all examined specimens.

For the CST samples, the distribution of elements was not uniform; consequently, the amount of different oxides formed during the HT differed at the examined points.

The surface of the first cast alloy, CST1 (Figure 3a), reflected the microstructure of the grains coated with oxides. Some parts of the areas were enriched with Cr, Si, and W and slightly lower in Co (according to the EDS results (Figure 3b,d)). The same regularity occurred in the oxides' distribution—the amount of CoO, Cr<sub>2</sub>O<sub>3</sub>, WO<sub>3</sub>, and SiO<sub>2</sub> formed during the HT differs in the examined spots (Figure 3c).

The oxide layer covering the CST2 sample replicated a typical dendritic structure featuring a dendritic matrix and interdendritic areas with some precipitations visible despite the HT effects (Figure 4a). The interdendritic areas also presented an inhomogeneous structure consisting of small, rounded, bright inclusions (an arrow in Figure 4d) and grey zones.

Unevenly distributed Co, Cr, Mo, W, and Si characterized the oxides covering the surface of CST2 according to the surface chemical composition tests (the maps presenting the surface composition, points, and linear distribution of particular elements—Figure 4b–d, respectively). Co and Cr mainly concentrated in the oxides covering the matrix space, while the oxides covering the interdendritic zones were enriched with Mo, W, and Si. The observation remains in compliance with the content of MoO<sub>3</sub>, WO<sub>3</sub>, SiO<sub>2</sub>, and Cr<sub>2</sub>O<sub>3</sub> measured in the marked spots (Figure 4c). The areas of rounded precipitations were highly enriched with Cr, W, and Si. The distribution of oxygen shows its increased content in the dendritic zones (Figure 4d).

The oxidized surface of the MSM sample is shown in Figure 5a. A layer consisting of the same type of oxides covers the surface. Bolder oxides, probably along the grain boundaries of the base alloy, could also be observed. Pores of diffuse distribution were also visible.

The results of chemical microanalysis showed a more uniform arrangement of Co, Cr, Mo, Si, and oxygen (Figure 5b,d) when both CST samples were compared. Additionally, the differences in the amount of oxides present at the marked points on the surface were less significant (Figure 5c).

The microstructures of the oxide layers covering both SLM specimens were much more uniform than those observed on the cast specimens' surfaces (Figures 6a and 7a). An inconsiderable amount of randomly distributed small pores was also visible.

In the specimen SLM1 after HT, the oxide layer was continuous, and bolder oxides covered the alloys' grain boundaries. The EDS studies (both presenting the surface distribution (Figure 6b) and line profile of the elements (Figure 6d)) showed a higher content of Cr and O and a lower content of Co and Mo in the oxides forming the layer over the grain

boundaries. These conclusions corresponded with the results concerning the amount of CoO, Cr<sub>2</sub>O<sub>3</sub>, and MoO<sub>3</sub> in the marked spots (Figure 6c).

Similarities in the oxides' microstructure and the Cr, O, Co, and Mo distributions were evidenced by the SLM2 specimen (Figure 7b,d), where the distributions of W and Si are also similar to those of Co and Mo (Figure 7d). The amount of Cr<sub>2</sub>O<sub>3</sub> was higher in the oxides covering the boundary areas, while the content values of CoO, WO<sub>3</sub>, MoO<sub>3</sub>, and SiO<sub>2</sub> remained lower, contrary to the oxides covering the grain areas (Figure 7c).

### 3.2. Corrosion Properties Examinations

The values of corrosion current density  $j_{\text{corr}}$ , corrosion potential  $E_{\text{corr}}$ , and polarization resistance  $R_p$  for all examined samples are presented in Table 5.

**Table 5.** The corrosion parameters obtained for the examined alloys in 0.9% NaCl solution with reference to the saturated calomel electrode (SCE) in potential range from  $-1$  to  $2$  V.

Sample	$j_{\text{corr}}$ [A/cm <sup>2</sup> ]	$E_{\text{corr}}$ [V]	$R_p$ [Ohm/cm <sup>2</sup> ] $\cdot 10^3$
CST1	$5.65 \times 10^{-7} \pm 0.19$	$-0.464 \pm 0.016$	$46.632 \pm 0.055$
CST2	$4.07 \times 10^{-6} \pm 0.14$	$-0.524 \pm 0.011$	$15.662 \pm 0.0085$
MSM	$2.6 \times 10^{-7} \pm 0.07$	$-0.481 \pm 0.009$	$99.774 \pm 0.0017$
SLM1	$2.05 \times 10^{-7} \pm 0.08$	$-0.324 \pm 0.005$	$168.114 \pm 0.096$
SLM2	$4.2 \times 10^{-8} \pm 0.2$	$-0.459 \pm 0.003$	$652.988 \pm 0.138$

Potentiodynamic characteristics for polarization in the range from  $-1.0$  to  $2.0$  V in a semi-logarithmic arrangement are presented in Figure 8.

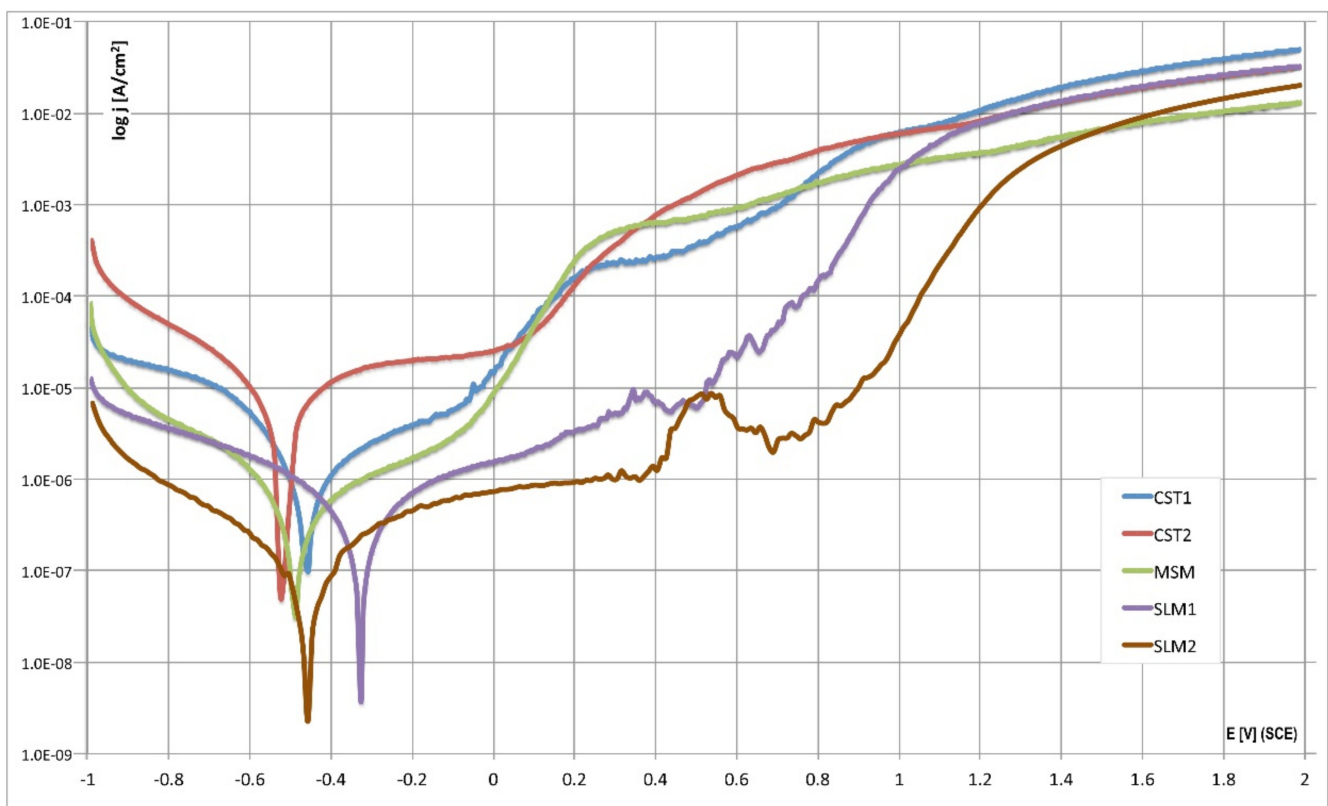


**Figure 8.** Potentiodynamic curves obtained for examined samples.

The values of the potential at which the corrosion current increased suddenly (the so-called breakdown potential  $E_{\text{br}}$ ), as shown in Table 6.

**Table 6.** Values of the breakdown potential calculated from the potentiodynamic curves.

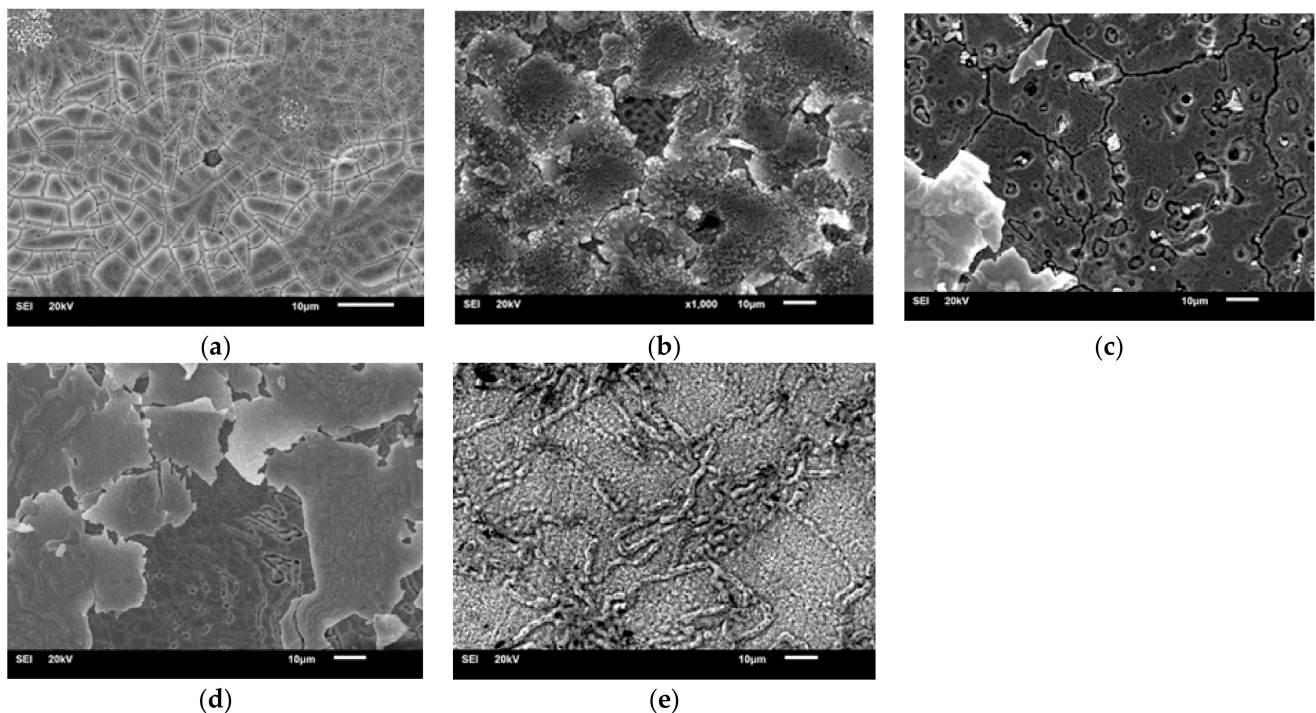
Sample	CST1	CST2	MSM	SLM1	SLM2
E <sub>br</sub> [V]	$-0.129 \pm 0.007$	$0.108 \pm 0.006$	$-0.054 \pm 0.003$	$0.320 \pm 0.0015$	$0.428 \pm 0.0025$

According to Table 5, CST2 presented the highest corrosion current density ( $j_{\text{corr}} = 5.65 \times 10^{-7} \pm 0.19 \text{ A/cm}^2$ ). The SLM2 sample had the best corrosion results, with a corrosion current density equal to  $4.2 \times 10^{-8} \pm 0.2 \text{ A/cm}^2$ . The potentiodynamic curves for SLM alloys were the most shifted in the right direction. During the anodic scan, the values of the passive currents were lower in comparison to those of the CST samples and the MSM specimen.

The so-called breakdown potential's value was another parameter used for evaluating corrosion resistance. It was demonstrated by a significant increase in the current in the anodic domain. The breakdown potential was more anodic for SLM2 than for other samples ( $E_{\text{br}} = 0.428 \pm 0.0025 \text{ V}$ ) and lowest in CST1 (being equal to  $-0.129 \pm 0.007 \text{ V}$  (Table 6)).

For all examined data ( $j_{\text{corr}}$ ,  $E_{\text{corr}}$ ,  $R_p$ , and  $E_{\text{br}}$ ), the p-value corresponding to the F-statistic of the one-way ANOVA was lower than 0.05, suggesting that one or more treatments were significantly different. The Tukey post-hoc test identified that, for  $j_{\text{corr}}$ ,  $R_p$ , and  $E_{\text{br}}$ , all of the pairs of treatments were significantly different from each other. For  $E_{\text{corr}}$ , in CST1 and SLM2 treatments, there was no significant difference.

The microstructures of the alloys after potentiodynamic polarization tests are shown in Figure 9a–e. Additionally, Figure 10 presents the results of the EDS line profile obtained for the CST1 sample. Figures 11–14 show the point analysis results for the rest of the oxidized samples after CT (in points marked on the SEM-SE images).

**Figure 9.** SEM SE images of samples' surfaces after CT: (a) CST1; (b) CST2; (c) MSM; (d) SLM1; (e) SLM2.

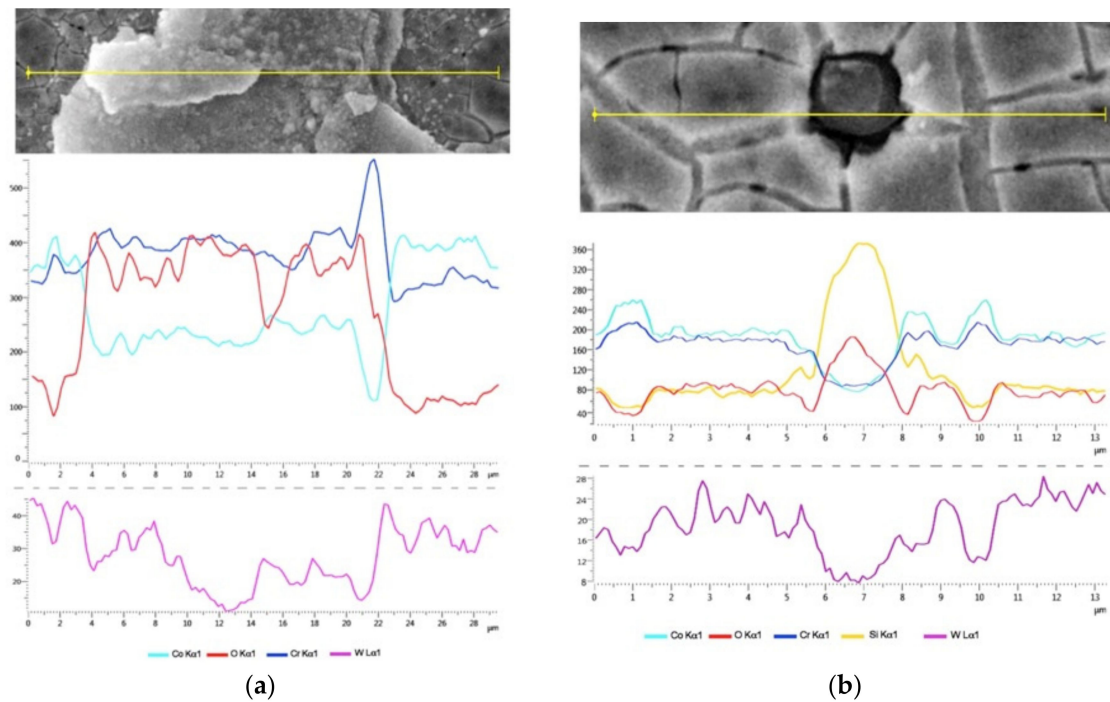
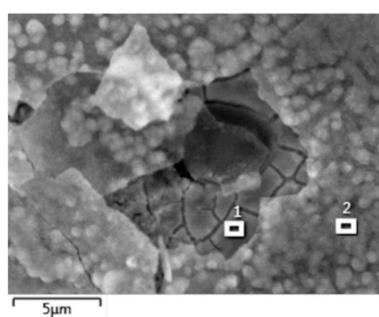
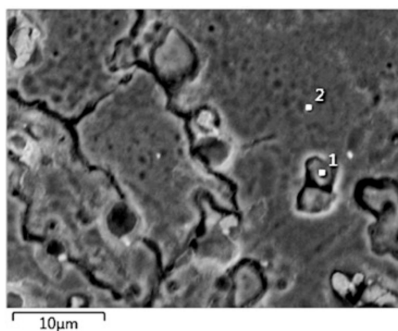


**Figure 10.** SEM-SE micrograph of CST1 with corresponding EDS line scan results: (a) along two oxide layers; (b) through the precipitation.



Element [wt %]	Point 1	Point 2	Oxide [wt %]	Point 1	Point 2
O	32.95	35.27			
Si	0.5	1.02	SiO <sub>2</sub>	1.06	2.19
Cr	19.89	28,64	Cr <sub>2</sub> O <sub>3</sub>	33.69	46.92
Fe	0.32	0,24	FeO	0.42	0.3
Co	34.38	26.36	CoO	48.66	39,17
Mo	4.48	3.11	MoO <sub>3</sub>	6.73	4.67
W	7.48	5.36	WO <sub>3</sub>	9.44	6.76
Total:	100	100		100	100

**Figure 11.** Results of EDS point analyses for the CST2 sample after corrosion examinations with a chart comparing oxide content.



Element [wt %]	Point 1	Poin t 2	Oxide [wt%]	Point 1	Point 2
O	25.38	25.88			
Si	0.62	0.48	SiO <sub>2</sub>	1.32	1.03
Cr	17.71	21.66	Cr <sub>2</sub> O <sub>3</sub>	25.88	31.66
Mn	0.33	0.58	MnO	0.43	0.75
Co	50.63	46.12	CoO	64.37	58.64
Mo	5.33	5.28	MoO <sub>3</sub>	8.0	7.92
Total:	100	100		100	100

**Figure 12.** Results of EDS point analyses for MSM sample after corrosion examinations.

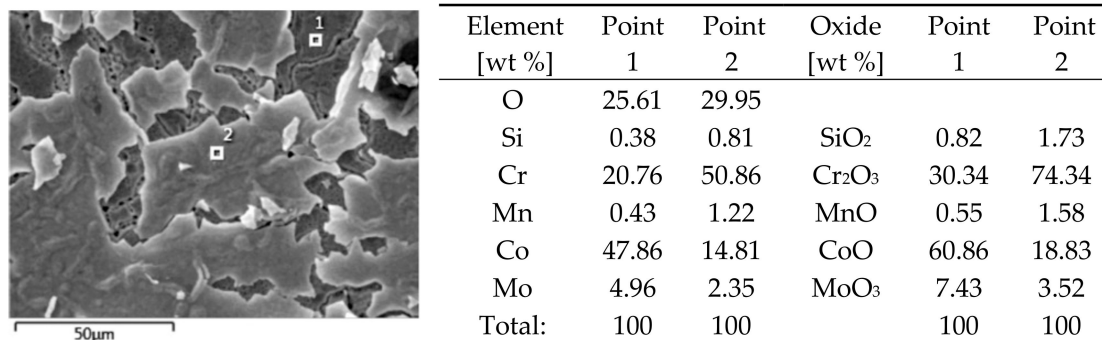


**Figure 13.** Results of EDS point analyses for the SLM1 sample after corrosion examinations.

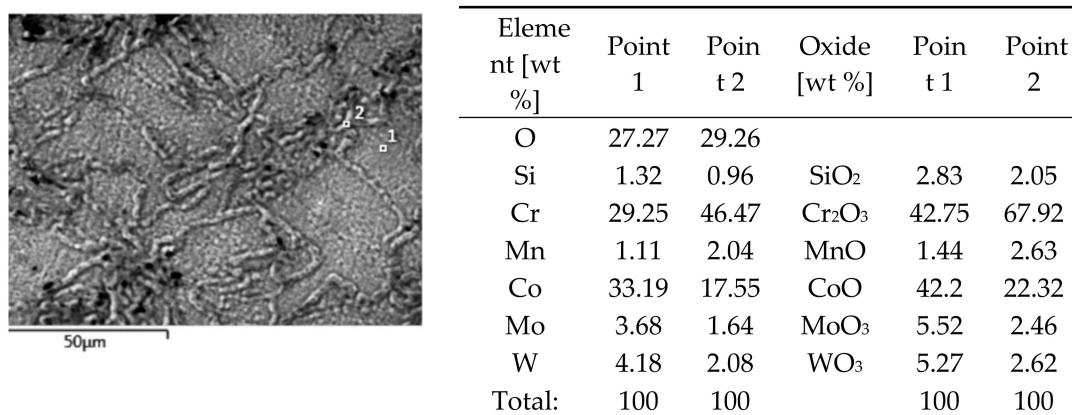


**Figure 14.** Results of EDS point analyses for the SLM2 sample after corrosion examinations.

Figure 9a–f presents the state of the samples' surfaces after the corrosion tests (CT). The surface damage with corrosion pits could be observed only in the CST2 sample (Figure 9b).

The areas covered by a cracked oxide layer were visible on the surface of the CST1, CST2, MSM, and SLM1 samples (Figure 9a–d). Signs of slight “etching” occurred around the pores present on the MSM surface. The uniform oxide layer, similar to the one created after the HT, covered the surface of the SLM2 sample (Figure 9e).

The CST1 alloy was covered by cracked oxides, with some randomly distributed areas of outer, flake-like-shaped oxides located on the inner cracked layer. The EDS line analysis (Figure 10a,b) demonstrated the presence of Cr, O, Co, and W with a fairly even distribution (taking into account different oxides' thicknesses along the analyzed line). The rounded precipitation (Figure 10b) in the central part of the analyzed line probably demonstrated an oxide rich in Si, covering the Si-rich phase that was present in the primary alloy structure.

The surface of the electrochemically tested CST2 alloy was also covered by a cracked oxide layer mainly made of CoO and Cr<sub>2</sub>O<sub>3</sub> (Figure 11). The upper oxide layer had a higher amount of SiO<sub>2</sub> and a lower quantity of MoO<sub>3</sub> in comparison to the inner one.

The appearance and distribution of oxides appeared to be similar in the MSM alloy's surface after CT; however, the quantity of external oxides was decreased. Some signs of preferential dissolution at the grain boundaries could be observed in the MSM sample after corrosion tests (Figure 12), but there was no evidence of typical corrosion damage. Moreover, the type and amount of oxides present at different points on the surface remained similar (Figure 12).

The microstructure and chemical composition of the oxides examined at representative points of the SLM1 surface after CT (Figure 13) confirmed that the flake-shaped upper oxides were enriched with the Cr<sub>2</sub>O<sub>3</sub> oxide and depleted of CO.

The microstructure of the SLM2 surface (Figure 14) remained almost the same as it had been before the CT. There was no evidence of a flake-shaped upper oxide layer or any

corrosion signs. The composition of oxides in the bolder layer was the same as it was inside of the grains.

#### 4. Discussion

Some studies investigated the impact of HT (being the result of porcelain firing) on the corrosion properties of dental base metal alloys obtained by different technologies. The high temperature reached during porcelain firing caused the creation of oxide layers, which in turn influenced the alloys' corrosion resistance. Different manufacturing methods leading to different alloys' morphologies may change the nature of the surface oxidation, hence influencing their corrosion performance.

The corrosion of Co–Cr dental alloys in the oral environment was inhibited by the existence of a Cr oxide layer on the surface [27,32,33]. Thus, it was crucial to determine how the structure of an alloy (which depends on the manufacturing method) influences the structure of the oxide/oxide layer formed during the HT.

In the CST1 sample, typical dendritic grains dominated before the HT (Figures 1a and 2a), and the intermetallic phases were precipitated along the grain boundaries. Cr, W, and Si were unevenly distributed in cobalt. The structure of the above cast alloy was described in the literature [34–36] as coarse-grained with solidification segregation that results in inhomogeneous material quality.

The microstructure of the oxide layer covering the CST1 (as a result of the HT) consisted of oxides presenting varied amounts of Cr, Si, W, and Co. The amount of CoO, Cr<sub>2</sub>O<sub>3</sub>, WO<sub>3</sub>, and SiO<sub>2</sub> formed during the HT was different in the examined spots. Considering these results, we assumed that the structure of the oxide layer examined in the present study (Figure 3b–d) partly reflected the microstructure of the alloy before the HT.

An analysis of the microstructure of the untreated CST2 along with the results of the EDS tests (Figures 1b and 2b) revealed that the sample presented a matrix featuring a typical dendritic band structure, in addition to the interdendritic precipitations of irregular size. Apart from the inhomogeneous dendritic structure typical for cast elements, the CST2 also contained precipitations rich in Mo, W, and Si. Wylie et al. stated that Mo moves from the solid solution of dental alloys to the precipitations nucleating at the junction of the second phase and the matrix. Thus, their presence is considered undesirable because they deteriorate the corrosion resistance [36]. Mo is a common addition to alloys and promotes resistance to pitting and crevice corrosion. Y.S. Al Jabbari, T. Matkovic, and Karpuschewski et al. [37–39] described the presence of said kinds of precipitations and their negative effect on corrosion resistance and mechanical properties.

The oxidized CST2 specimen retained a dendritic solidification microstructure with more pronounced dendrites as well as precipitates enriched with W, Mo, and Si (Figure 4a–d). The inhomogeneous oxide layer, created as a result of the HT, affected the low corrosion resistance of the CST2 sample examined in the present paper.

This conclusion remains in accordance with results obtained by Xin et al. [40]. They investigated the characteristics of the surface and corrosion behavior of cast and SLM cobalt–chromium (Co–Cr) alloys before and after PFM firing. After the test, it was stated that both groups preserved the structure that they had before the HT.

Qiu et al. (who examined the corrosion behavior and surface properties of cast Co–Cr and two Ni–Cr dental alloys before and after simulated porcelain firing) also proved that the firing process had little effect on the microstructure of the Co–Cr alloy, since no homogenization was detected in the microstructure of the Co–Cr alloy. The examined specimens showed a noticeable dendritic structure with interdendritic areas and precipitations [14]. Ardlin, Dahl, and Tibballs investigated the structure and corrosion behavior of different dental alloys (among which were Co–Cr base alloys) before and after oxidation, simulating the temperature cycles for the application of ceramic to metal. They stated that the heating cycle did not appear to affect the Co–Cr base alloys' microstructure [41].

The MSM alloy examined in this study was produced by the use of technology based on powder metallurgy methods. These methods, compared to traditional casting, enabled

us to achieve a product with a more cognate structure (also confirmed in this paper) [42]. The MSM before the HT presented a structure that was common for sintered material, i.e., with grains of different sizes and pores present both in grain boundaries and inside the grains (Figure 1c). Pores were attributed to the necking of metallic powder during sintering and the possible remainder of the organic binder; their presence was also reported in other studies [43,44]. The distribution of Co, Cr, and Mo was even, according to the EDS results (Figure 2c).

The MSM alloy sample after the HT showed no changes in the chemical composition of the oxide layers covering the surface, apart from the appearance of oxygen (following the EDS maps of element distribution and the linear and point analyses from chosen areas (Figure 5a–d)). The distribution of Co, Cr, and Mo was also more uniform in the sintered sample, which indicated a more homogeneous composition of oxides than the ones that form on CST alloys. Pores were distributed in both visible grains and grain boundaries.

Before the HT, the SLM1 alloy displayed a homogeneous microstructure consisting of grains of different size with small pores and some bright, rounded precipitations (Figure 1d). The result of EDS line scans along the line crossing this phase indicated a higher amount of Mo and Si and a decrease in Co (Figure 2f). Apart from that, the distribution of the elements was uniform (Figure 2d).

The primary microstructure of SLM2 alloy consisted of grains with arch-shaped boundaries (Figure 1e). The sample presented a uniform distribution of all examined elements (Figure 2e).

As described in the Results section, both thermally treated SLM alloys (SLM1, Figure 6a–d, and SLM2, Figure 7a–d) showed a homogeneous oxide microstructure, and a small amount of randomly distributed pores was also detected. The chemical compositions of the oxide layers proved that the main phases were  $\text{Cr}_2\text{O}_3$  and  $\text{CoO}$ . The microstructure of both SLM samples was characterized by the oxides' swellings present in the grain boundary regions. The compositions of the oxides at the points located in the grain boundaries and grains showed no difference. Moreover, the highest percentage of  $\text{Cr}_2\text{O}_3$  among all alloys analyzed occurred in the SLM samples (Table 4).

Considering the microstructures of the oxide layers covering the examined alloys after the HT, we can conclude that all specimens retained their structure. This statement is in accordance with the results obtained by Jabbari et al. [3], who compared the microstructure, porosity, mechanical properties, ion release, and tarnish resistance of Co–Cr alloys developed by conventional casting (CST), milling (MIL), selective laser melting (SLM), and milling soft metal (MSM). They concluded, among others, that the thermal treatment of porcelain firing did not affect the microstructural features of CST, MIL, and SLM groups. Additionally, Li et al., who investigated the bond strengths of porcelain to cobalt-chromium alloys made by casting, milling, and selective laser melting, stated that the microstructures of the cast, milled, and SLM alloys did not differ after porcelain firing [31].

The authors of the present study characterized oxide layers on the surfaces of thermally treated alloys in order to identify differences in their composition and structure to consider whether and how these diversities explain their different corrosive behavior. The investigations confirmed significant differences in the surface microstructure of the oxidized cast, sintered, and laser-sintered samples visible after HT simulating porcelain firing. The SLM technique and MSM method revealed a homogeneous oxide structure, contrary to both cast specimens. The porosity was observed in all groups of specimens, although SLM provided structures with limited internal porosity. The random slight porosity observed for the SLM samples was probably caused by an incorrect adjustment of operating conditions, and this was also reported by others [45,46].

All of the examined samples formed chromium oxide films, but other metallic elements were present in the oxides, especially the ones that covered the second phases of the CST1 and CST2 alloys.

The studies available in the literature were mostly focused on the influence of different modifications in alloys' compositions on the corrosion resistance after oxidation, rather

than on the effect of the primary microstructure on their corrosion behavior after the HT. For example, K. Yamanaka et al. [28,29] described the effects of the addition of silicon and boron on oxide films formed on Co–Cr–W base dental alloys at 1273 K for 15 min in air. They proved that the addition of Si and B could make the dense Cr<sub>2</sub>O<sub>3</sub> phase resistant to changes and restrict the formation of Co oxides. Y. Lu et al. investigated the oxidation behavior of Co–Cr–W alloys with Cu additions and stated that Cu content in the film structure could affect the thickness of the Cr oxide regions, accelerating the oxidation of Co–Cr–W alloys [45].

Other studies concerning the impact of production methods and various HT parameters were mainly aimed at assessing the quality of the connection with ceramics, but the conclusions on the structure of oxides could also be relevant to corrosive considerations. J. Li et al. concluded that predominantly Cr oxides were formed on the Co–Cr alloys' surface during oxidizing HT and reported that similar morphologies and similar amounts of oxides were observed for the cast and milled alloy surfaces [31]. These conclusions were partly in contrast to the ones presented in this article; however, the CNCM (computer numerical control milling) method was also based on casting technology. Serra-Prat et al. compared the shear bond strength of dental porcelain to cast, milled, and laser-sintered cobalt-chromium alloys. They reported that differences in alloy microstructures caused by different manufacturing methods might also simultaneously change the nature of surface oxidation, significantly modifying adhesion behavior as a result [46].

In the present article, conclusions concerning the microstructures of oxidized surfaces are reflected in the corrosion examination results (Tables 5 and 6; Figures 8–14).

The determination of *icorr* and *Ecorr* values was carried out in a narrow range of potentials (as described in the methodology), but the paper presents only *icorr* and *Ecorr* values obtained from the extrapolation of "Tafel regions", but no graphs (graphic results) of polarization curves considered adequate for Tafel extrapolation were published.

Considering the results of the statistical analysis, the null hypothesis could be rejected. Thick oxides, forming inner and outer cracked layers, covered all examined alloys after the CT, except for the SLM2. Hodgson et al. described similar microstructures of anodically polarized Co–Cr alloys [47]. They examined the passive and transpassive behavior of alloys and showed that the oxide film became significantly thicker, a change in its composition took place, and the dissolution rate increased in the transpassive region. In the passive region, Cr was present in the film mainly as Cr(III) oxide and with a small amount of Cr(III) hydroxide. The studies performed by the authors indicated that (at transpassive potentials) a thick and unstable oxide film (not highly protective) constantly covered the surface.

The current densities, while the anodic polarization was stopped at a potential equal to 2 V, were the same in the CST2 and SLM1 alloys and equal to  $3 \times 10^{-2}$  A/cm<sup>2</sup>. While comparing the morphologies of these alloys, it was observed that, contrary to CST2, the SLM1 alloy did not exhibit any localized corrosion damage (Figure 9a,b,d).

Less evident but also comparable current densities were found for the SLM2 and MSM alloys (with values of  $1.4 \times 10^{-2}$  A/cm<sup>2</sup> and  $2 \times 10^{-2}$  A/cm<sup>2</sup>) with polarizations equal to 2 V. In these cases, the corrosion morphology was different (Figure 9c,e).

The potentiodynamic polarization tests allowed us to state that the corrosion resistance of the SLM and MSM alloys after HT was improved in comparison to the cast samples (CST1 and CST2).

According to the values of the corrosion parameters obtained, corrosion resistance decreased in the following order: SLM2 > SLM1 > MSM > CST1 > CST2. The shapes of all potentiodynamic curves remained similar and typical for passive materials. The values of the passive currents for the SLM alloys were lower in comparison to the CST samples and MSM specimens, proving an improved protection efficiency not only in the corrosion potential domain, but also in the passive potential range. A transpassive area, with a significant increase in the anodic current, followed the passive range of the anodic curve. Eliaz, who described passivity and its breakdown of Co–Cr biomaterials, explained that the

current increase was due to transpassive dissolution by oxidation of the passive  $\text{Cr}_2\text{O}_3$ -rich film into soluble  $\text{CrO}_4^{2-}$  species and was not related to pitting corrosion [48].

The increase in the breakdown potential  $E_{br}$  for the SLM alloys proved that a homogeneous structure of oxides improved their corrosion resistance.

The results of the potentiodynamic polarization tests demonstrated that the corrosion potentials of the SLM alloys shifted to more positive values, and the corrosion current densities were lower in comparison to the MSM and cast alloys. The SLM1 and SLM2 alloys exhibited a similar corrosion behavior, and their higher corrosion resistance can be attributed to the homogeneous oxide layer formed during the HT process. We assumed that the last one is the result of the homogeneous structure of the alloy.

In the course of the curves for SLM1 and SLM2 samples obtained by laser sintering, temporary increases in the current values are visible in the area of potentials above  $\sim 0.35$ – $0.45$  V. The surface of the samples “at the entrance” was covered with oxides from the firing simulation process. This phenomenon may be related to the partial transformation process—the transition of Cr to a higher oxidation state (corresponding to the oxidation reactions of Cr at a higher valence level. (Dissolution by oxidation of the  $\text{Cr}_2\text{O}_3$ -rich passive film into soluble  $\text{CrO}_4^{2-}$  species). There have been reports of this type concerning the behavior of Co–Cr–Mo alloys using potentiodynamic studies in the potential ranges of 500–700 mV in HBSS, where the authors explained the occurring increases in the value of currents by the transition of chromium to a higher degree of oxidation in oxides. Further research and immersion tests at peak potentials will allow to investigate these new products.

Additionally, the results of the potentiodynamic polarization test for the oxidized MSM alloy indicated an improved corrosion resistance in comparison to the cast specimens. The related literature included only studies evaluating the structure and corrosion resistance of non-thermally treated MSM elements. The results of these studies revealed that MSM alloys present a more improved corrosion resistance than casting alloys, due to the uniformity of the structure. H. Kim et al. [49] compared the microstructure and in vitro biocompatibility of Co–Cr alloys fabricated by casting and MSM methods. They reported that the microstructure of the MSM specimen was characterized by a fine grain size structure and showed consistently significantly smaller releases of Co ions in comparison with cast specimens. D. Rylska et al. conducted examinations of the structure and corrosion resistance of MSM Co–Cr base elements and confirmed that the sintered alloy exhibited better self-passivating behavior in comparison to cast material [50].

The thermally treated MSM alloy exhibited a lower corrosion resistance than the SLM alloys, despite exhibiting a substantial homogeneous distribution of elements in the oxide layer (Figure 5b–d). The possible reason for reduced corrosion resistance may be the porosity in the MSM alloy’s structure. The existence of a direct correlation between pores and corrosion resistance was already discussed in other studies and remains in accordance with the results of the present study. For example, Buciumeanu et al. reported decreased corrosion resistance of hot-pressed Co–Cr alloys related to their increasing porosity [51]. Krasicka et al. investigated the corrosion properties of sintered compacts made of a Co–Cr–Mo alloy and concluded that the structure and porosity of the materials influenced the corrosion resistance of the investigated samples [52]. They revealed that these sintered specimens did not exhibit typical passive behavior or a current plateau in the passive region in the anodic polarization curves. They also showed that the examined compacts had higher passive current densities in the passive range than cast alloys. The authors suggested that the higher values of the passive current densities for the sintered samples were the result of their real surface areas, which were higher than the nominal areas. This conclusion may be also relevant to the present study.

Cast alloys after the HT, especially CST2, exhibited lower corrosion resistance. The oxide layer covering the CST1 surface was characterized by an uneven distribution of elements with areas enriched with Co and depleted of Cr, W, and Si (according to the EDS

results; Figure 3b,d). Such distribution influenced the corrosion resistance (Tables 5 and 6; Figure 8).

The CST2 coarse-grained structure with microsegregation in dendrites and inclusions such as intermetallic phases (Figures 1b and 2b) influenced the kind and distribution of oxides formed after the HT. The presence of oxides of various compositions was responsible for the lowest corrosion resistance, which was confirmed in the results of corrosion tests. The CST2 alloy presented the highest  $j_{\text{CORR}}$  and the lowest  $E_{\text{br}}$  among the examined specimens (Tables 5 and 6; Figure 8).

These results were in line with the conclusions presented by X-Z. Xin et al. [4]. They reported that, following firing, SLM samples made of Co–Cr alloys displayed significantly improved corrosion resistance compared with traditional cast specimens at pH 2.5. Microstructural differences between oxidized cast and SLM alloys and a thicker oxide layer on SLM explained the improved corrosion resistance on the surface of SLM specimens.

## 5. Conclusions

Within the limitations of this study, the main results can be concluded as follows:

1. The corrosion resistance after HT simulating porcelain firing was affected by the microstructure of the oxides covering surface of alloys.
2. For cast alloys, the coarse secondary phases were detrimental to the formation of protective homogeneous oxide films. The highest resistance to corrosion after the HT was observed in SLM alloys due to the microstructural homogeneity of the oxide layers.
3. The lowest corrosion resistance of cast alloys after HT was a result of their inhomogeneous oxide layers. In terms of the MSM alloy, the lower corrosion resistance may be caused by the porosity.
4. The structure of oxides forming during PFM processes reflected the morphology of the primary alloys.

Some issues require more detailed approach and attention and they are:

1. We are aware that the methods and kinds of apparatus used in the present study, e.g., scanning electron microscopy and EDS, were inadequate for detailed examinations of oxide layers.
2. Further research is needed to obtain more precise information about oxide layer structures and compositions (for example, X-ray photoelectron spectroscopy). Such research, which would include cross-section examinations, will enable us to compare the thicknesses of oxide layers on the surfaces of Co–Cr alloys and determine the possible relationship between oxide thickness and the primary alloy's structure.
3. Further investigations should also be focused on simulating the high chemical aggression of physiological fluids in the oral cavity. Many factors can change the pH of saliva, in ranges between 3.5 and 8.3, and the pH of saliva may contribute to the corrosion of dental implants.
4. The next objective would be to characterize the effect of saliva pH on the passive behavior of these alloys after PFM.
5. The authors are aware that with such a small number of tests, the test power allows only to determine that the results are not varied by accident. Increasing sample size will boost the statistical power of the tests carried. The current study should be considered as a pilot study and further investigations should be focused on the minimum number of groups (for example only SLM group with CST group as a control one) with increased sample size.

From the practical point of view, the conducted experiments provide, in the humble opinion of the authors, a valuable results on the influence of manufacturing method, which strongly affects the structure of tested materials and therefore their corrosion behavior, which can strongly affect their usefulness in dental applications.

**Author Contributions:** Conceptualization: J.S. and D.R.; methodology: J.S. and D.R.; validation: J.S. and D.R.; formal analysis: D.R., B.J., and G.S.; investigation: D.R. and B.J.; resources: J.S., D.R., and G.S.; writing—original draft preparation: D.R.; writing—review and editing: D.R.; visualization: D.R.; supervision: J.S. All authors have read and agreed to the published version of the manuscript.

**Funding:** This research received no external funding.

**Institutional Review Board Statement:** Not applicable.

**Informed Consent Statement:** Not applicable.

**Data Availability Statement:** Data sharing not applicable.

**Conflicts of Interest:** The authors declare no conflict of interest.

## References

1. Wu, Y.; Moser, J.B.; Jameson, L.M.; Malone, W.F.P. The effect of oxidation heat treatment on porcelain bond strength in selected base metal alloys. *J. Prosthet. Dent.* **1991**, *66*, 439–444. [[CrossRef](#)]
2. Suleiman, S.H.; von Steyrn, P.V. Fracture strength of porcelain fused to metal crowns made of cast, milled or laser-sintered cobalt-chromium. *Acta Odontol. Scand.* **2013**, *71*, 1280–1289. [[CrossRef](#)]
3. Al Jabbari, Y.S.; Barmpagadaki, X.; Psarris, I.; Zinelis, S. Microstructural, mechanical, ionic release and tarnish resistance characterization of porcelain fused to metal Co–Cr alloys manufactured via casting and three different CAD/CAM techniques. *J. Prosthodont. Res.* **2019**, *63*, 150–156. [[CrossRef](#)]
4. Kovalev, A.; Mishina, V.; Titov, V.; Moiseev, V.; Tolochko, N. Selective laser sintering of steel powders to obtain products based on SAPR models. *Metallurgist* **2000**, *4*, 206–209. [[CrossRef](#)]
5. Iseri, U.; Ozkurt, Z.; Kazazoglu, E. Shear strengths of veneering porcelain to cast, machined and laser-sintered titanium. *Dent. Mater. J.* **2011**, *30*, 274–280. [[CrossRef](#)]
6. Metikos-Hukovic, M.; Babic, R. Passivation and corrosion behaviours of cobalt and cobalt-chromium-molybdenum alloy. *Corros. Sci.* **2007**, *49*, 3570–3579. [[CrossRef](#)]
7. Manaranche, C.; Hornberger, R. A proposal for the classification of dental alloys according to their resistance to corrosion. *Dent. Mater.* **2007**, *23*, 1428–1437. [[CrossRef](#)]
8. Chang, J.-C.; Oshid, Y.; Gregory, R.L.; Andres, C.J.; Barco, T.M.; Brown, D.T. Electrochemical study on microbiology-related corrosion of metallic dental materials. *BioMed. Mater. Eng.* **2003**, *13*, 281–295. [[PubMed](#)]
9. Johnson, T.; Van Noort, R.; Stokes, C.W. Surface analysis of porcelain fused to metal systems. *Dent. Mater.* **2006**, *22*, 330–337. [[CrossRef](#)]
10. Eschler, P.Y.; Reclaru, L.; Luthy, H.; Blatter, A.; Larue, C.; Susz, C.; Bosch, J. Corrosion Testing of Cobalt-Chromium Dental Alloys doped with Precious Metals. *Eur. Cells Mater.* **2005**, *26*, 4358–4365.
11. Milosev, I. The effect of biomolecules on the behaviour of CoCrMo alloy in various simulated physiological solutions. *Electrochim. Acta* **2012**, *78*, 259–273. [[CrossRef](#)]
12. Bauer, S.; Schmuki, P.; Von der Mark, K.; Park, J. Engineering biocompatible implant surfaces. Part I: Materials and surfaces. *Prog. Mater. Sci.* **2013**, *58*, 261–326. [[CrossRef](#)]
13. Sang-Bae, L.; Ju-hye, L.; Woong-Chul, K.; Sae-Yoon, O.; Kyoung-Nam, K.; Ji-Hwan, K. Effect of different oxidation treatments on the bonding strength of new dental alloys. *Thin Solid Films* **2009**, *517*, 5370–5374.
14. Qiu, J.; Yu, W.-Q.; Zhang, F.-Q.; Smales, R.J.; Zhang, Y.-L.; Lu, C.-H. Corrosion behaviour and surface analysis of a Co–Cr and two Ni–Cr dental alloys before and after simulated porcelain firing. *Eur. J. Oral Sci.* **2011**, *119*, 93–101. [[CrossRef](#)]
15. Li, X.; He, J.; Zhang, W.; Jiang, N.; Li, D. Additive manufacturing of biomedical constructs with biomimetic structural organizations. *Materials* **2016**, *9*, 909. [[CrossRef](#)]
16. Vandenbroucke, B.; Kruth, J.P. Selective laser melting of biocompatible metals for rapid manufacturing of medical parts. *Rapid Prototyp. J.* **2007**, *13*, 196–203. [[CrossRef](#)]
17. Kim, K.B.; Kim, W.C.; Kim, H.Y.; Kim, J.H. An evaluation of marginal fit of three unit fixed dental prostheses fabricated by direct metal laser sintering system. *Dent. Mater.* **2013**, *29*, 91–96. [[CrossRef](#)]
18. Xin, X.Z.; Chen, J.; Xiang, N.; Wei, N. Surface properties and corrosion behaviour of Co–Cr alloy fabricated with selective laser melting technique. *Cell Biochem. Biophys.* **2013**, *67*, 983–990. [[CrossRef](#)]
19. Tuna, S.H.; Pekmez, N.Ö.; Kürkcüo, I. Corrosion resistance assessment of Co–Cr alloy frameworks fabricated by CAD/CAM milling, laser sintering, and casting methods. *J. Prosthet. Dent.* **2015**, *114*, 725–734. [[CrossRef](#)]
20. Krug, K.P.; Knauber, A.W.; Nothdurft, F.P. Fracture behaviour of metal-ceramic fixed dental prostheses with frameworks from cast or a newly developed sintered cobalt-chromium alloy. *Clin. Oral Investig.* **2015**, *19*, 401–411. [[CrossRef](#)]
21. Li, K.C.; Prior, D.J.; Waddell, J.N.; Swain, M.V. Comparison of the microstructure and phase stability of as-cast, CAD/CAM and powder metallurgy manufactured Co–Cr dental alloys. *Dent. Mater.* **2015**, *31*, 306–315. [[CrossRef](#)]
22. Adzali, N.M.S.; Jamaludin, S.B.; Derman, M.N. Effect of Sintering on the Physical and Mechanical Properties of Co–Cr–Mo (F-75)/HAP Composites. *Sains Malays.* **2013**, *42*, 1763–1768.

23. Quante, K.; Ludwig, K.; Kern, M. Marginal and internal fit of metal–ceramic crowns fabricated with a new laser melting technology. *Dent. Mater.* **2008**, *24*, 1311–1315. [[CrossRef](#)] [[PubMed](#)]
24. Akova, T.; Ucar, Y.; Tukay, A.; Balkaya, M.C.; Brantley, W.A. Comparison of the bond strength of laser-sintered and cast base metal dental alloys to porcelain. *Dent. Mater.* **2008**, *24*, 1400–1404. [[CrossRef](#)] [[PubMed](#)]
25. Xiang, N.; Xin, X.Z.; Chen, J.; Wei, B. Metal–ceramic bond strength of Co–Cr alloy fabricated by selective laser melting. *J. Dent.* **2012**, *40*, 453–457. [[CrossRef](#)] [[PubMed](#)]
26. Castillo-Oyague, R.; Osorio, R.; Osorio, E.; Sanchez-Aguilera, F.; Toledano, M. The effect of surface treatments on the micro roughness of laser-sintered and vacuum-cast base metal alloys for dental prosthetic frameworks. *Microsc. Res. Tech.* **2012**, *75*, 1206–1212. [[CrossRef](#)] [[PubMed](#)]
27. Koutsoukis, T.; Zinelis, S.; Eliades, G.; Al-Wazzan, K.; Rifaiy, M.A.; Al Jabbari, Y.S. Selective laser melting technique of Co–Cr dental alloys: A review of structure and properties and comparative analysis with other available techniques. *J. Prosthodont.* **2015**, *24*, 303–312. [[CrossRef](#)]
28. Yamanaka, K.; Mori, M.; Ohmura, K.; Chiba, A. Preventing high-temperature oxidation of Co–Cr-based dental alloys by boron doping. *J. Mater. Chem.* **2016**, *4*, 309–317. [[CrossRef](#)]
29. Yamanaka, K.; Mori, M.; Chiba, A. Surface characterisation of Ni-free Co–Cr–W-based dental alloys exposed to high temperatures and the effects of adding silicon. *Corros. Sci.* **2015**, *94*, 411–419. [[CrossRef](#)]
30. Li, J.; Ye, X.; Li, B.; Liao, J.; Zhuang, P.; Ye, J. Effect of oxidation heat treatment on the bond strength between a ceramic and cast and milled cobalt–chromium alloys. *Eur. J. Oral Sci.* **2015**, *123*, 297–304. [[CrossRef](#)]
31. Li, J.; Chen, C.; Liao, J.; Liu, L.; Ye, X.; Lin, S.; Ye, J. Bond strengths of porcelain to cobalt–chromium alloys made by casting, milling, and selective laser melting. *J. Prosthet. Dent.* **2017**, *118*, 69–75. [[CrossRef](#)] [[PubMed](#)]
32. Saji, V.-S.; Choe, H.-C. Electrochemical behaviour of Co–Cr and Ni–Cr dental cast alloys. *Trans. Nonferrous Met. Soc. China* **2009**, *19*, 785–790. [[CrossRef](#)]
33. Hsua, R.W.W.; Yang, C.C.; Huang, C.A.; Chen, Y.S. Electrochemical corrosion studies on Co–Cr–Mo implant alloy in biological solutions. *Mater. Chem. Phys.* **2005**, *93*, 531–538. [[CrossRef](#)]
34. Yamanaka, K.; Mori, M.; Kuramoto, K.; Chiba, A. Development of new Co–Cr–W-based biomedical alloys: Effects of microalloying and thermomechanical processing on microstructures and mechanical properties. *Mater. Des.* **2014**, *55*, 987–998. [[CrossRef](#)]
35. Yamanaka, K. Influence of carbon addition on mechanical properties and microstructures of Ni-free Co–Cr–W alloys subjected to thermomechanical processing. *J. Mech. Behav. Biomed. Mater.* **2014**, *37*, 1751–1616. [[CrossRef](#)] [[PubMed](#)]
36. Wylie, C.M.; Shelton, R.M.; Fleming, G.J.; Davenport, A.J. Corrosion of nickel-based dental casting alloys. *Dent. Mater.* **2007**, *23*, 714–723. [[CrossRef](#)]
37. Al Jabbari, Y.S.; Koutsoukis, T.; Barmpagadaki, X.; Zinelis, S. Metallurgical and interfacial characterization of PFM Co–Cr dental alloys fabricated via casting, milling or selective laser melting. *Dent. Mater.* **2014**, *30*, 79–88. [[CrossRef](#)] [[PubMed](#)]
38. Matkovic, T.; Matkovic, P.; Malina, J. Effects of Ni and Mo on the microstructure and some other properties of Co–Cr dental alloys. *J. Alloys Compd.* **2004**, *366*, 197–293. [[CrossRef](#)]
39. Karpuschewski, B.; Pieper, H.J.; Krause, M.; Doring, J. CoCr is not the same: CoCr-blanks for dental machining. In *Future Trends in Production Engineering*; Schuh, G., Neugebauer, R., Uhlmann, E., Eds.; Springer: Berlin/Heidelberg, Germany, 2013; pp. 261–274.
40. Xin, X.-Z.; Che, J.; Xiang, J.; Gong, Y.; Wei, B. Surface characteristics and corrosion properties of selective laser melted Co–Cr dental alloy after porcelain firing. *Dent. Mater.* **2014**, *30*, 263–270. [[CrossRef](#)]
41. Ardlin, B.I.; Dahl, J.E.; Tibballs, J.E. Static immersion and irritation tests of dental metal–ceramic alloys. *Eur. J. Oral Sci.* **2005**, *113*, 83–89. [[CrossRef](#)]
42. Kim, H.R.; Jang, S.H.; Kim, Y.K.; Son, J.S.; Min, B.K.; Kim, K.H. Microstructures and mechanical properties of Co–Cr dental alloys fabricated by three CAD/CAM-based processing techniques. *Materials* **2016**, *9*, 596. [[CrossRef](#)] [[PubMed](#)]
43. Takaichi, A.; Suyalatu, S.; Nakamoto, T.; Natsuka, J.; Nomura, N.; Tsutsumi, Y.; Migita, S.; Doi, H.; Kurosu, S.; Chiba, A.; et al. Microstructures and mechanical properties of Co-29Cr-6Mo alloy fabricated by selective laser melting process for dental applications. *J. Mech. Behav. Biomed. Mater.* **2013**, *21*, 67–76. [[CrossRef](#)] [[PubMed](#)]
44. Reclaru, L.; Ardelean, L.; Rusu, L.C.; Sinescu, C. Co–Cr material selection in prosthetic restoration: Laser sintering Technology. *Solid State Phenom.* **2012**, *188*, 412–415. [[CrossRef](#)]
45. Lu, Y.; Lin, W.; Xie, M.; Xu, W.; Liu, Y.; Lin, J.; Yu, C.; Tang, K.; Liu, W.; Yang, K.; et al. Examining Cu content contribution to changes in oxide layer formed on selective-laser-melted CoCrW alloys. *Appl. Surf. Sci.* **2019**, *464*, 262–272. [[CrossRef](#)]
46. Serra-Prat, J.; Cano-Batalla, J.; Cabratosa-Termes, J.; Figueras-Álvarez, O. Adhesion of dental porcelain to cast, milled, and laser-sintered cobalt–chromium alloys: Shear bond strength and sensitivity to thermocycling. *J. Prosthet. Dent.* **2014**, *112*, 600–605. [[CrossRef](#)] [[PubMed](#)]
47. Hodgson, A.W.E.; Kurz, S.; Virtanen, S.; Fervel, V.; Olsson, C.-O.A.; Mischler, S. Passive and transpassive behaviour of CoCrMo in simulated biological solutions. *Electrochim. Acta* **2004**, *49*, 2167–2178. [[CrossRef](#)]
48. Eliaz, N. Corrosion of Metallic Biomaterials: A Review. *Materials* **2019**, *12*, 407. [[CrossRef](#)]
49. Kim, H.R.; Kim, Y.K.; Son, J.S.; Min, B.K.; Kim, K.-H.; Kwon, T.-Y. Comparison of in vitro biocompatibility of a Co–Cr dental alloy produced by new milling/post-sintering or traditional casting technique. *Mater. Lett.* **2016**, *178*, 300–303. [[CrossRef](#)]
50. Rylska, D.; Sokołowski, G.; Konieczny, B.; Sokołowski, J. The structure and corrosive properties of the CoCr-base dental alloy obtained by soft material milling followed by sinterization. *J. Achiev. Mater. Manuf. Eng.* **2016**, *2*, 60–71. [[CrossRef](#)]

- 
51. Buciumeanu, M.; Bagheri, A.; Souza, J.C.M.; Silva, F.S.; Henriques, B. Tribocorrosion behavior of hot pressed CoCrMo alloys in artificial saliva. *Tribol. Int.* **2016**, *97*, 423–430. [[CrossRef](#)]
  52. Krasicka-Cydzik, E.; Oksiuta, Z.; Dabrowski, J.R. Corrosion testing of sintered samples made of the Co-Cr-Mo alloy for surgical applications. *J. Mater. Sci. Mater. Med.* **2005**, *16*, 97–202. [[CrossRef](#)] [[PubMed](#)]